Applied Surface Science 459 (2018) 309–317

Contents lists available at ScienceDirect

Applied Surface Science

journal homepage: www.elsevier.com/locate/apsusc

Full Length Article

# Mesoporous reduced graphene oxide/$WSe_2$ composite particles for efficient sodium-ion batteries and hydrogen evolution reactions

Jung Sang Cho[a,b,1], Seung-Keun Park[a,c,1], Kyung Min Jeon[a], Yuanzhe Piao[d,e,*], Yun Chan Kang[a,*]

[a] Department of Materials Science and Engineering, Korea University, Anam-Dong, Seongbuk-Gu, Seoul 136-713, Republic of Korea
[b] Department of Engineering Chemistry, Chungbuk National University, Republic of Korea
[c] Department of Chemical Engineering, Kongju National University, Budae-Dong 275, Chungnam 314-701, Republic of Korea
[d] Program in Nano Science and Technology, Graduate School of Convergence Science and Technology, Seoul National University, 145 Gwanggyo-ro, Yeongtong-Gu, Suwon, Gyeonggi-do 443-270, Republic of Korea
[e] Advanced Institutes of Convergence Technology, 145 Gwanggyo-ro, Yeongtong-Gu, Suwon, Gyeonggi-do 443-270, Republic of Korea

ARTICLE INFO

*Keywords:*
Tungsten selenide
Sodium ion batteries
Hydrogen evolution
Graphene
Spray pyrolysis

ABSTRACT

Mesoporous $WSe_2$-reduced graphene oxide ($WSe_2$-rGO) composite particles were prepared by spray pyrolysis and subsequent selenization. The $WSe_2$-rGO composite particles had both well-dispersed rGO nanosheets and well-faceted $WSe_2$ nanocrystals with plenty of folded edges. As a comparison sample, hierarchical structured $WSe_2$ particles were produced by selenization of the bare $WO_3$ particles obtained by spray pyrolysis. The $WSe_2$-rGO composite particles showed superior electrochemical properties for sodium-ion batteries (SIBs) and electrocatalytic efficiencies for hydrogen evolution reactions (HERs) compared to those of the bare $WSe_2$ particles. The discharge capacities of the $WSe_2$-rGO composite particles and bare $WSe_2$ particles for the 100th cycle at a current density of 0.5 A $g^{-1}$ for sodium-ion storage were 238 and 36 mA h $g^{-1}$, respectively; their corresponding capacity retentions measured from the third cycle were 80% and 13%. The $WSe_2$–rGO composite particles showed much lower onset potential and larger current density (36.5 mA $cm^{-2}$ at $\eta$ = 300 mV) than those of the bare $WSe_2$ particles (0.61 mA $cm^{-2}$ at $\eta$ = 300 mV). The Tafel slopes for the $WSe_2$–rGO composite and bare $WSe_2$ particles were approximately 60 and 115 mV $dec^{-1}$, respectively.

## 1. Introduction

Layer-structured transitional metal dichalcogenides (TMDs) have recently attracted increasing attention because of their distinctive electronic, catalytic, optical, and electrochemical properties [1–7]. TMDs ($MX_2$ where M = Mo, W and X = S, Se) have a structure similar to graphite because they are composed of hexagonal metal atoms (M) sandwiched between two chalcogen atom (X) layers. Additionally, there is strong covalent bonding within the M–X–M layers, with only fairly weak van der Waals interactions between neighboring sandwich layers [8–11].

$MoS_2$, $MoSe_2$, $WS_2$, and $WSe_2$ materials with various morphologies have been extensively studied as anode materials for lithium- and sodium-ion batteries, and as electrocatalysts for hydrogen evolution reactions (HERs) [12–19]. Accordingly, tungsten diselenide ($WSe_2$) could be used in the above applications. The unique $WSe_2$ structure is expected to allow for the insertion and extraction of relatively large $Na^+$ ions compared to $Li^+$ ions present between the layers without any significant volume changes [20,21]. In particular, the nanostructured $WSe_2$-graphene composite materials could be well applied as electrocatalysts for both HERs and anode materials for sodium-ion batteries (SIBs).

Graphene is expected to improve the electrical conductivities of the nanostructured $WSe_2$ materials. However, $WSe_2$ materials have been scarcely studied up till now. Share et al. investigated the sodium-ion storage performance of the bulk $WSe_2$ material [22]. A reversible capacity above 200 mA h $g^{-1}$ was observed at a 20 mA $g^{-1}$ rate. Zhang et al. synthesized carbon-coated $WSe_2$ nanomaterials by solid-state reaction. The $WSe_2$/C nanomaterials showed a reversible sodium storage capacity of 270 mA h $g^{-1}$ after 50 cycles without any notable loss [23]. Wang et al. investigated the electrocatalytic performances of the aligned $WSe_2$ nanofilms on Si nanowires and a carbon fiber paper [24].

* Corresponding authors at: Program in Nano Science and Technology, Graduate School of Convergence Science and Technology, Seoul National University, 145 Gwanggyo-ro, Yeongtong-Gu, Suwon, Gyeonggi-do 443-270, Republic of Korea (Y. Piao). Department of Materials Science and Engineering, Korea University, Anam-Dong, Seongbuk-Gu, Seoul 136-713, Republic of Korea (Y.C. Kang).
*E-mail addresses:* parkat9@snu.ac.kr (Y. Piao), yckang@korea.ac.kr (Y.C. Kang).
[1] These authors contributed equally to this work.

https://doi.org/10.1016/j.apsusc.2018.07.200
Received 12 February 2018; Received in revised form 11 July 2018; Accepted 29 July 2018
Available online 30 July 2018

The $WSe_2$ nanofilms on the carbon fiber paper acted as a highly efficient electrocatalyst for HERs compared to flat substrates. Liu et al. studied $WSe_2$ layers anchored on graphene sheets as the electrocatalyst for HERs [25]. The $WSe_2$/graphene hybrid exhibited excellent electrocatalytic activity in the HER, such as a low onset overpotential of −100 mV, a small Tafel slope of 64 mV per decade, and outstanding stability.

In this study, nanostructured $WSe_2$-reduced graphene oxide ($WSe_2$-rGO) composite particles with spherical particles of fine size were prepared for the first time by a simple two-step process. Precursor $WO_3$-rGO composite particles were prepared by spray pyrolysis and they were subsequently transformed into $WSe_2$-rGO composite particles by a simple selenization process. The electrochemical properties of SIBs and electrocatalytic efficiencies for the HERs of the $WSe_2$-rGO composite were compared to those of the bare $WSe_2$ particles prepared by the same process without applying graphene oxide (GO).

## 2. Experimental

Mesoporous $WSe_2$-rGO composite particles were prepared by a two-step process. In brief, the procedure for the particles by spray pyrolysis used a solution containing ammonium metatungstate hydrate $[(NH_4)_6H_2W_{12}O_{40}{\cdot}xH_2O]$ and GO nanosheets (Fig. S1) (see supplementary data). The preparation procedure of GO nanosheets are described in our previous reports [26,27]. The reactor temperature and flow rate of $N_2$ gas during the spray pyrolysis were fixed at 500 °C and 7 L $min^{-1}$, respectively. To prepare $WSe_2$-rGO composite particles, the as-prepared $WO_3$-rGO composite particles were selenized at 500 °C for 12 h under a 10% $H_2$/Ar reducing atmosphere with selenium metal particles. Bare $WSe_2$ particles without rGO were also prepared as a comparison sample. Precursor $WO_3$ particles, prepared by spray pyrolysis, were selenized under identical post treatment conditions as those mentioned above. For simplicity, the $WSe_2$-rGO composite particles and bare $WSe_2$ particles without rGO are referred to as "$WSe_2$-rGO" and "bare $WSe_2$", respectively. Detailed characterization method, sodium ion battery and electrochemical measurements procedures are described in the Supporting Information.

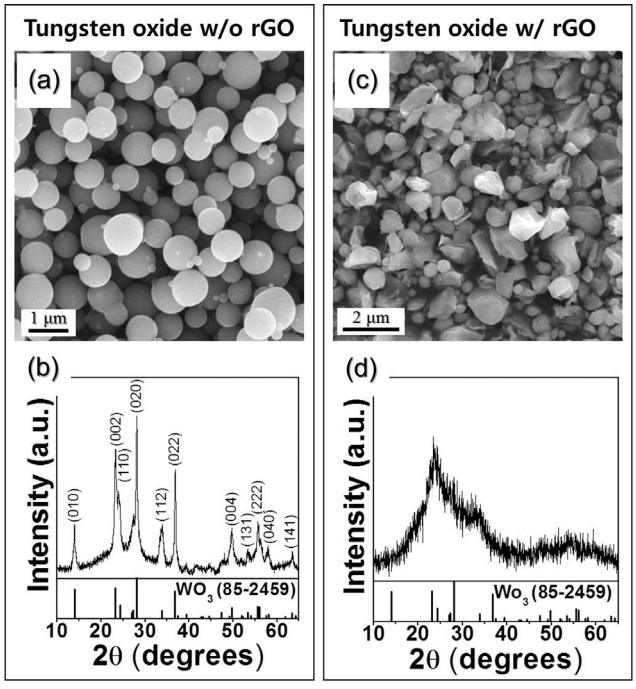


**Fig. 1.** SEM images and XRD patterns of the (a and b) bare $WO_3$ particles without rGO and (c and d) $WO_3$–rGO composite particles prepared directly by spray pyrolysis process at 500 °C under $N_2$ gas atmosphere.

Supplementary data associated with this article can be found, in the online version, at https://doi.org/10.1016/j.apsusc.2018.07.200.

## 3. Results and discussion

The morphologies and X-ray diffraction (XRD) patterns of the tungsten oxide particles prepared directly by the spray pyrolysis process from the solution with and without GO are shown in Fig. 1. The particles prepared from the solution without GO were spherical and had a filled structure (Fig. 1a). However, GO uniformly dispersed in the droplet changed the morphology of the tungsten oxide particles into crumpled shapes, as shown in Fig. 1c. The XRD patterns of both particles exhibited diffraction peaks corresponding to the hexagonal phase of $WO_3$ (JCPDS no. 85–2459), irrespective of GO inclusion (Fig. 1b and d). However, mean sizes of the crystallite domains of the powders prepared from the solution with and without GO were estimated to be 3 and 26 nm, respectively, which are determined from Scherrer's formula. The obvious broadness of the XRD peaks of the sample with GO suggests that the crystallites are at the nanoscale level. During the spray pyrolysis process, GO was reduced to rGO by the thermal treatment at 500 °C under $N_2$ atmosphere. Therefore, the rGO sheet disturbed the crystal growth of the tungsten oxide formed through the decomposition

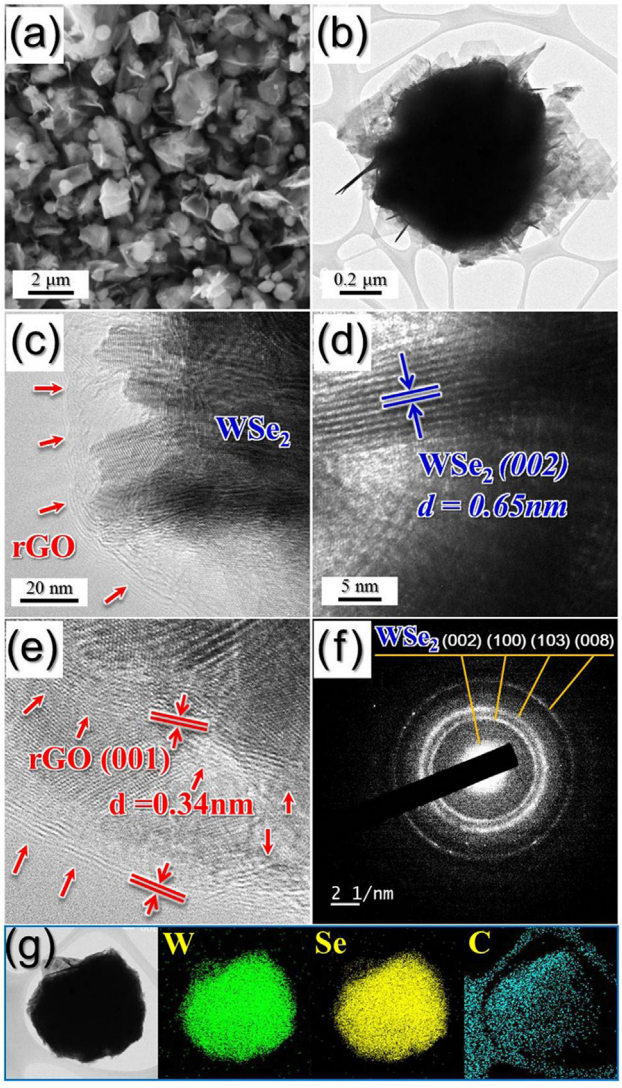


**Fig. 2.** Morphologies, SAED pattern, and elemental mapping images of the $WSe_2$–rGO composite microspheres after selenization at 500 °C: (a) SEM image, (b–e) TEM images, (f) SAED pattern, and (g) elemental mapping images.

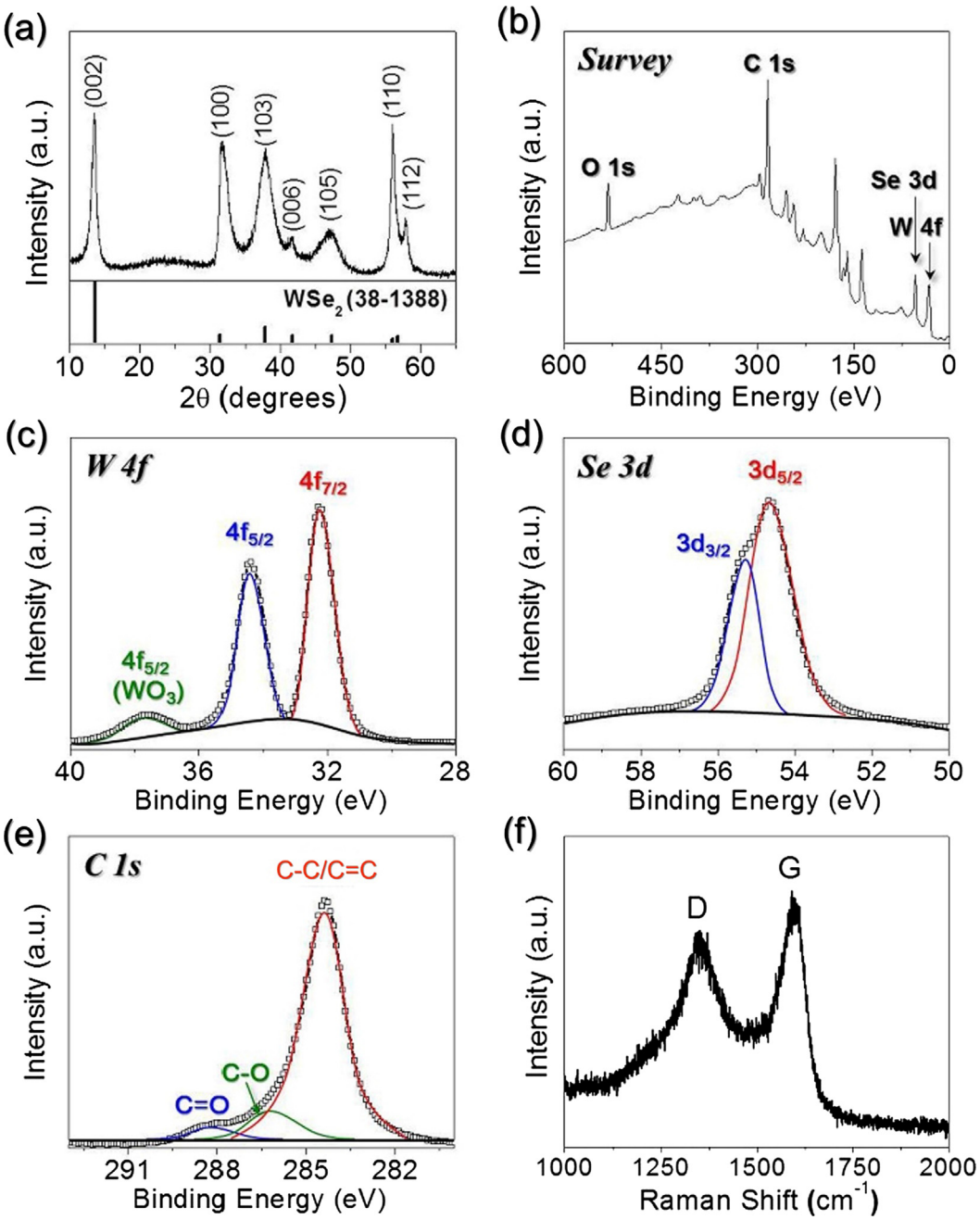


**Fig. 3.** XRD pattern, XPS spectra, and Raman spectrum of the $WSe_2$–rGO hybrid particles: (a) XRD pattern, (b) XPS survey spectrum, (c) XPS W 4f spectrum, (d) XPS Se 3d spectrum, (e) C 1s spectrum, and (f) Raman spectrum.

of ammonium metatungstate hydrate. Therefore, one $WO_3$-rGO composite particle with a low crystallite size was formed from each droplet by spray pyrolysis.

The morphology of the microstructure constructed with $WSe_2$ and rGO formed by the selenization process of the $WO_3$-rGO precursor particle is shown in Fig. 2. The ultrafine $WO_3$ nanocrystals embedded within the $WO_3$-rGO precursor particle transformed into the $WSe_2$ nanocrystals during the selenization process for 12 h at 500 °C. The particle morphology and size were mostly maintained even after the selenization process, as shown in Fig. 2a and b. The transmission electron microscopy (TEM) image (Fig. 2c) clearly shows that the particle is made of both well-faceted $WSe_2$ crystals with plenty of folded edges and rGO nanosheets. Interplanar spacings of 0.65 nm and 0.34 nm, which are consistent with the exposed edge sites of the (0 0 2) plane of the hexagonal $WSe_2$ phase and (0 0 1) plane of the rGO phase, respectively, were observed (Fig. 2d and e). The large interlayer distance between (0 0 2) planes offers enough space to accommodate $Na^+$ ions and gives rise to $Na^+$ ion diffusion channels. The selected area electron diffraction (SAED) and XRD patterns, shown in Figs. 2f and 3a, respectively, confirmed the formation of the $WSe_2$-rGO composite particles with pure $WSe_2$ crystal phase. The elemental mapping images, shown in Fig. 2g, revealed the uniform distribution of the pure $WSe_2$ nanocrystals and rGO sheets in the composite particle.

The surface compositions and chemical states of the porous $WSe_2$-rGO composite particles were examined via X-ray photoelectron spectroscopy (XPS) in Fig. 3b–e. The survey XPS spectrum (Fig. 3b) indicates the presence of W, Se, and C elements in the $WSe_2$-rGO composite particles, which is consistent with the EDS result (Fig. S2). In the W 4f spectrum of the $WSe_2$-rGO composite particles (Fig. 3c), the main peaks were observed at binding energies of 32.2 eV for W $4f_{7/2}$ and

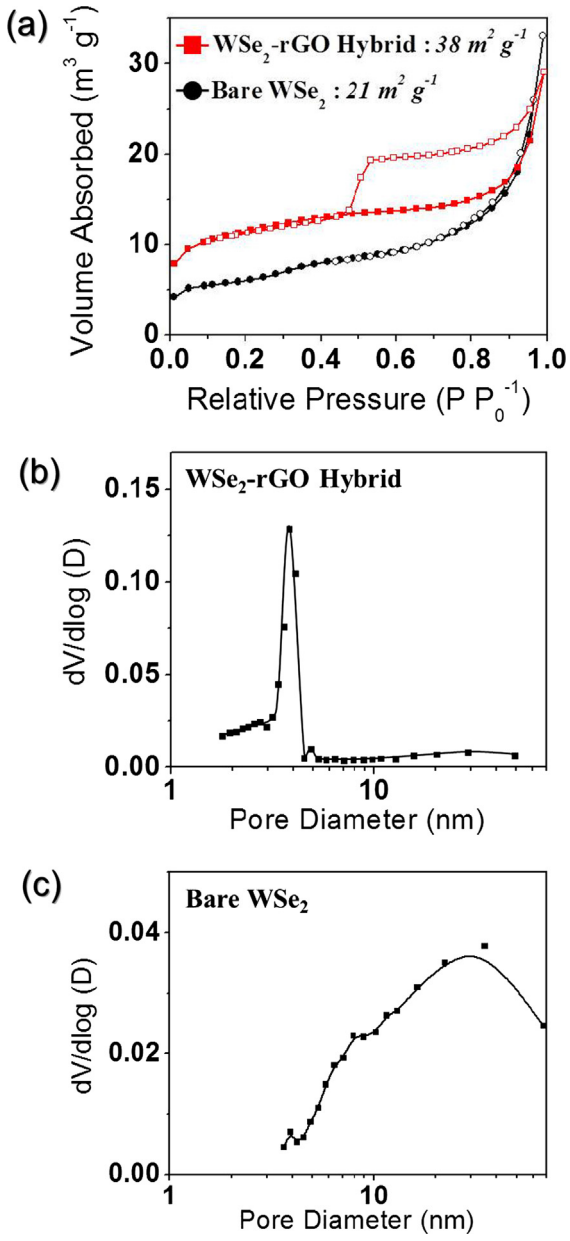


**Fig. 4.** (a) $N_2$ gas adsorption and desorption isotherms and pore size distributions of (b) the $WSe_2$–rGO composite and (c) the bare $WSe_2$ particles.

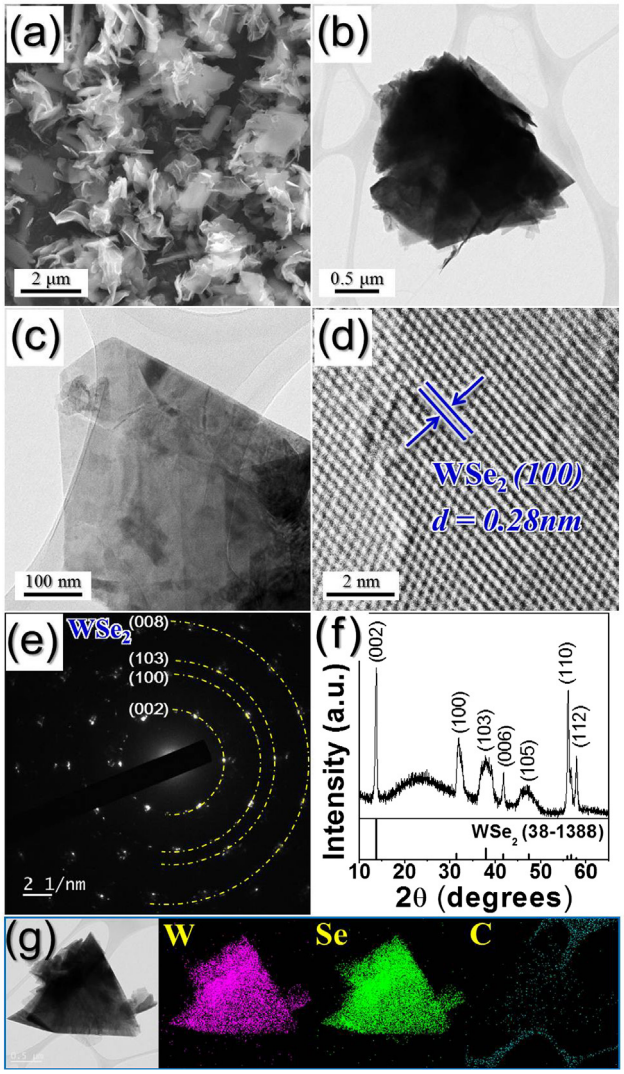


**Fig. 5.** Morphologies, SAED pattern, XRD pattern, and elemental mapping images of the bare $WSe_2$ particles after selenization at 500 °C: (a) SEM image, (b and c) TEM images, (d) HR-TEM image, (e) SAED pattern, (f) XRD pattern, and (g) elemental mapping images.

34.4 eV for W $4f_{5/2}$, which are the characteristic of $WSe_2$ [28,29]. The small peak at around 37.6 eV was assigned as W $4f_{5/2}$ and originated from the $WO_3$ phase due to the partial surface oxidation of the sample under an air atmosphere. This oxide phase is not detected by XRD analysis due to its amorphous nature [30]. In the Se 3*d* spectrum (Fig. 3d), Se $3d_{5/2}$ and Se $3d_{3/2}$ peaks were observed at 54.0 eV and 54.9 eV, respectively, which are also originated from the $WSe_2$ phase [28,29]. As shown in Fig. S3a, the C 1s spectrum of GO consists of three peaks which are C—C/C=C (284.4 eV), C—O (286.5 eV) and C=O (288.4 eV). The peak intensity of C—O is relatively high. After the pyrolysis, the peak intensity of oxygen-containing groups (C—O and C=O) is greatly reduced, indicating that most of oxygenated species are removed (Fig. 3e) [31,32]. The C—C bond exhibited the strongest intensity, which indicates that the GO nanosheets were thermally reduced to rGO nanosheets during the selenization process. The Raman spectrum, shown in Fig. 3f, contained the broad peaks at approximately ~1351 and ~1600 $cm^{-1}$, which correspond to the D (defect-related mode) and G ($E_{2g}$ graphitic mode) bands of the carbon material, respectively. The intensity ratio of D and G bands ($I_D/I_G$) provides useful information about the crystallinity degree of the rGO nanosheets [33,34]. The $I_D/I_G$ of the $WSe_2$-rGO composite particles was 0.84, indicating a lower crystallinity degree that can be ascribed to the presence of graphene layers. Meanwhile, the $I_D/I_G$ value of GO (1.17) was lower than that of the $WSe_2$-rGO composite due to numerous defects in graphitic networks which originated from oxidation process (Fig. S3b). The thermogravimetric (TG) curve of the $WSe_2$-rGO composite particles revealed the one-step weight loss for temperatures below 600 °C in Fig. S2b. It is attributed to the decomposition of $WSe_2$ to $WO_3$ and rGO combustion. The rGO content of 10 wt% in the $WSe_2$-rGO composite particles was estimated from the TG analysis. The $N_2$ adsorption and desorption isotherms of the $WSe_2$-rGO composite powders (Fig. 4a) had a clear hysteresis loop that resembled the type-H4 IUPAC (International Union of Pure and Applied Chemistry) isotherm classification [35]. This revealed the presence of mesopores within the $WSe_2$-rGO composite powders [36]. The Barrett-Joyner-Halenda (BJH) pore size distribution derived from the adsorption branch of the isotherm confirmed the well-developed mesopores in the $WSe_2$-rGO composite particles with a pore size between 3 and 4 nm (Fig. 4b and c). From the above analyses, it can be concluded that the mesoporous $WSe_2$-rGO composite particles could be prepared by a simple two-step process.

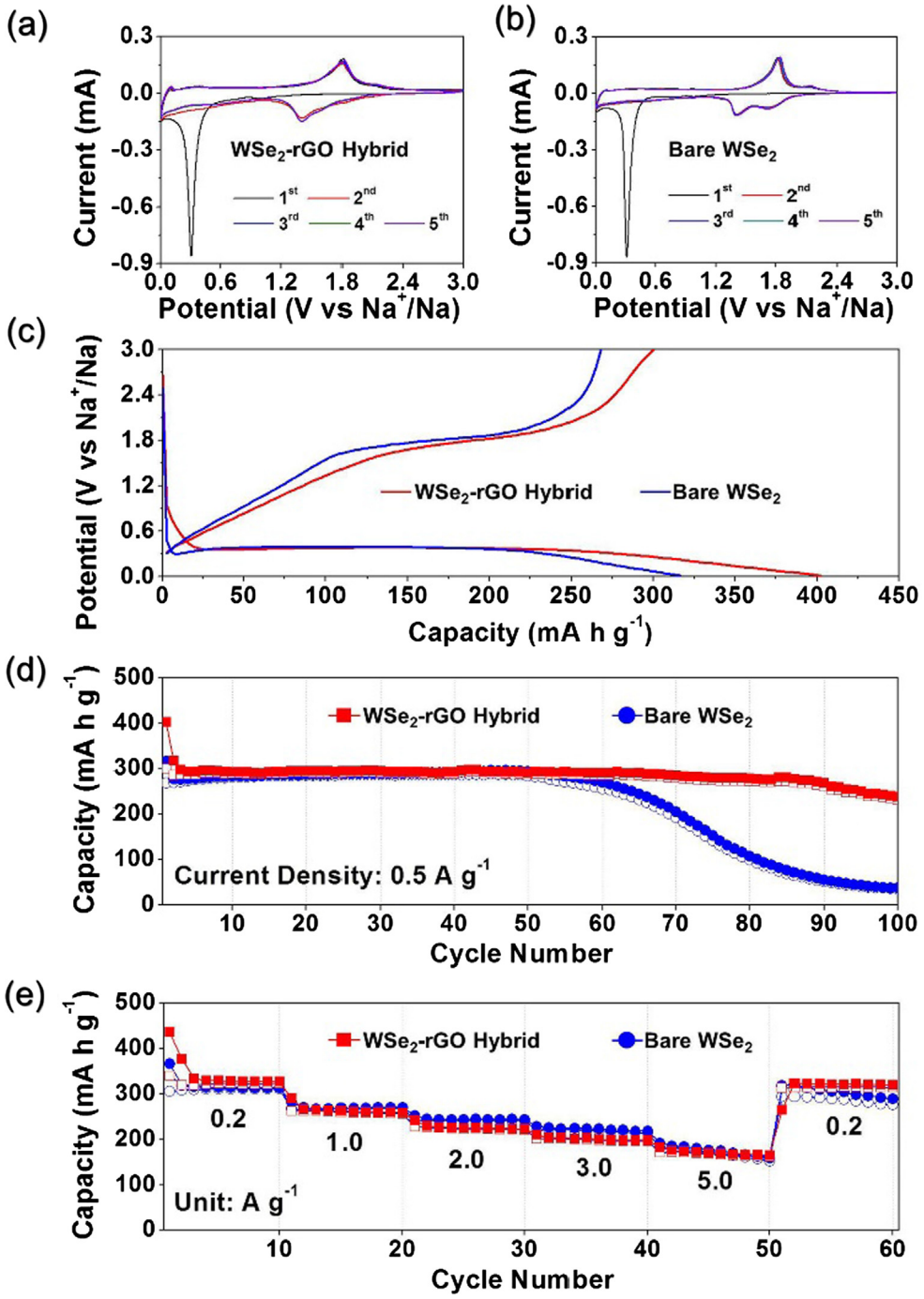


**Fig. 6.** Electrochemical properties of the $WSe_2$-rGO hybrid particles and bare $WSe_2$ particles: (a) CV curves of the $WSe_2$-rGO hybrid particles, (b) CV curves of the bare $WSe_2$ particles, (c) first charge-discharge curves at a current density of 0.5 A $g^{-1}$, (d) cycling performances at a current density of 0.5 A $g^{-1}$, and (e) rate performances.

The bare $WSe_2$ particles without rGO were also prepared as a comparison sample. The selenization process at 500 °C of the bare $WO_3$ particles produced the hierarchical structured $WSe_2$ particles, as shown in Fig. 5. The growth of the layer-structured $WSe_2$ nanocrystals deformed the spherical shape of the precursor $WO_3$ particle particles. Ultrathin layered $WSe_2$ nanosheets composed the aggregates, as shown in Fig. 5a–c. The HR-TEM images in Fig. 5d showed (1 0 0) crystal plane of hexagonal $WSe_2$ with lattice fringes separated by 0.28 nm. The SAED and XRD patterns shown in Fig. 5e and f, respectively, showed the phase-pure $WSe_2$ particles formation. The elemental mapping images also confirmed the complete conversion of $WO_3$ into $WSe_2$ during selenization (Fig. 5g).

The electrochemical properties of the mesoporous $WSe_2$-rGO composite particles for $Na^+$ ion storage were compared to those of the bare $WSe_2$ particles. The CVs of the two samples at a scan rate of 0.07 mV $s^{-1}$ during the first five cycles are shown in Fig. 6a and b. In both samples, a strong reduction peak at 0.31 V was observed in the first cathodic scan, which is attributed to the reaction of $WSe_2$ with $Na^+$ to form W and $Na_2Se$ [22,23]. After the second cycle onward, the cathodic peak shifted to the higher potential at 1.41 V due to the improved kinetics of the electrodes owing to the formation of ultrafine $WSe_2$ nanocrystals during the first cycling [37,38]. In bare $WSe_2$, two reduction peaks at high potentials of 1.41 and 1.72 V were observed from the second cycle, which were attributed to the conversion reaction

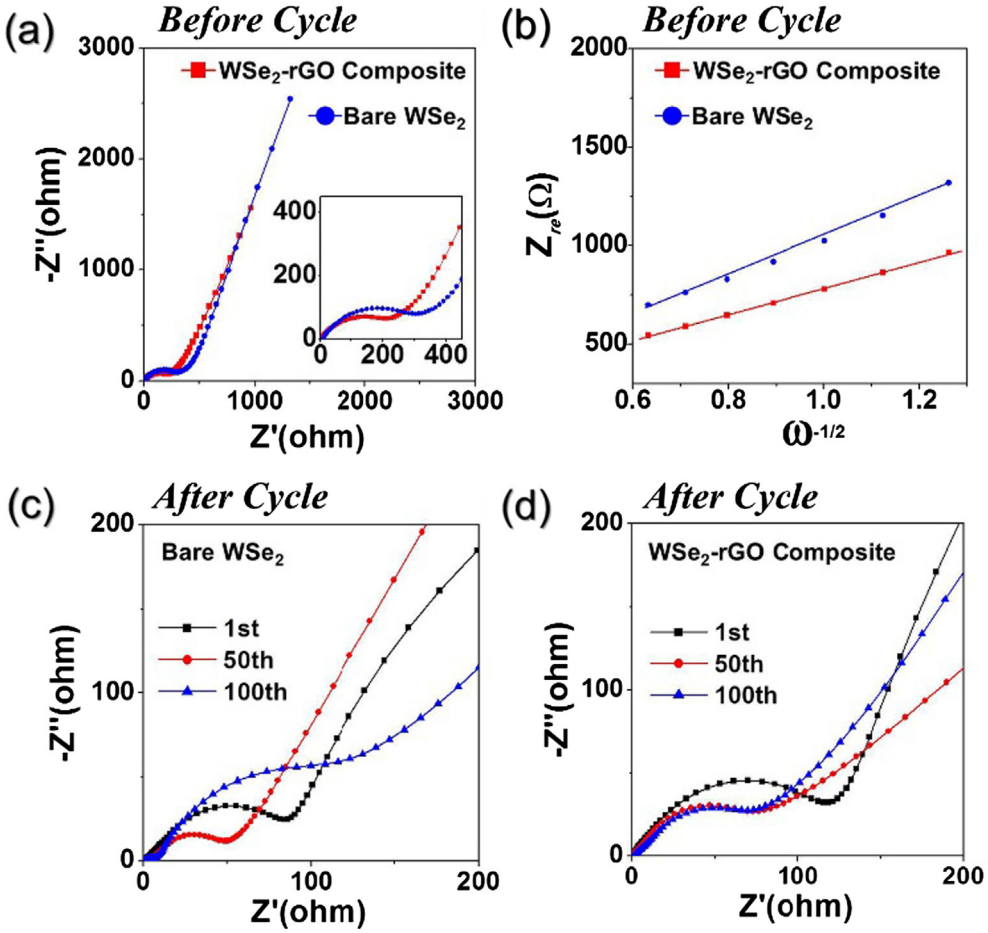


**Fig. 7.** (a, c, d) Nyquist impedance plots and (b) relationships between the real part of the impedance ($Z_{re}$) and $\omega^{-1/2}$ of the $WSe_2$-rGO hybrid particles and bare $WSe_2$ particles before and after cycling.

from $Na_xWSe_2$ to W and $Na_xSe$, respectively [22,23]. During the anodic scans, an oxidation peak at around 1.83 V was observed in the initial cycle of both samples, which could be attributed to the regeneration of W to $WSe_2$ nanograins [22,23]. The CV curves are substantially overlapped in the following cycles, suggesting good reversibility. Fig. 6c exhibited the initial discharge and charge profiles of the samples at a current density of 0.5 A $g^{-1}$. Both samples had similar shapes of discharge and charge curves. The clear plateaus at approximately 0.37 and 1.80 V were observed in the first discharge and charge curves, respectively. The $WSe_2$-rGO composite particles exhibited an initial discharge capacity of 402 mA h $g^{-1}$ and a charge capacity of 300 mA h $g^{-1}$, and the corresponding Coulombic efficiency was 75%. However, the initial discharge and charge capacities of the bare $WSe_2$ particles were 317 and 268 mA h $g^{-1}$, respectively, and their corresponding Coulombic efficiency was 85%. The $WSe_2$-rGO composite particles with higher specific surface area and fine crystallite size had higher capacities than those of the bare $WSe_2$ particles, although $WSe_2$-rGO composite particles contain rGO nanosheets with low capacity. However, the existence of rGO with high initial irreversible capacity loss resulted in lower initial Coulombic efficiency of the $WSe_2$-rGO composite particles than that of the bare $WSe_2$ counterpart. The cycle properties of the samples at a current density of 0.5 A $g^{-1}$ are shown in Fig. 6d. The $WSe_2$-rGO composite particles retained a high level of discharge capacity for 100 cycles, whereas the bare $WSe_2$ counterpart maintained the discharge capacities during the first 50 cycles and then decreased severely during the remaining 50 cycles. The discharge capacities of the $WSe_2$-rGO composite particles and bare $WSe_2$ particles for the 100th cycle were 238 and 36 mA h $g^{-1}$, respectively, and their corresponding capacity retentions measured from the third cycle were 80% and 13%. The rate performances of both samples are shown in Fig. 6e, in which the current density is increased step-wise from 0.2 to 5.0 A $g^{-1}$. Both samples showed similar good performances, irrespective of their morphologies and existence of rGO. The hierarchical and layered structure resulted in a good performance of the bare $WSe_2$ particles without high conductivity rGO nanosheets. The $WSe_2$-rGO composite particles had final discharge capacities of 327, 259, 223, 198, and 165 mA h $g^{-1}$ at current densities of 0.2, 1.0, 2.0, 3.0, and 5.0 A $g^{-1}$, respectively. When the current density decreased to 0.2 A $g^{-1}$, the original capacity of $WSe_2$-RGO hybrid almost recovered to 323 mA h $g^{-1}$ even after cycling at high current densities. In contrast, the capacity of bare $WSe_2$ gradually decreased under same condition. These results indicate that the $Na^+$ ion storage performance of $WSe_2$-rGO composite particles was not degraded at high current densities.

The electrochemical impedance spectroscopy (EIS) measurements before and after 1, 50, and 100 cycles were performed to investigate the superior $Na^+$ ion storage performance of the $WSe_2$-rGO composite particles. The Nyquist plots of the $WSe_2$ cells were taken by deconvolution with a Randle-type equivalent circuit model (Fig. S3), as shown in Fig. 7. The equivalent circuit model describes the electrochemical reaction steps [39,40]. The medium frequency semicircle in the Nyquist plots, shown in Fig. 7, was attributed to the charge-transfer resistance ($R_{ct}$) between the active material and the electrolyte [41–43]. The $WSe_2$-rGO composite particles, with high electrical conductivity, have a lower $R_{ct}$ value of 243 Ω than that of the bare $WSe_2$ particles before cycling (352 Ω), as shown in Fig. 7a. Fig. 7b shows the relationship between $Z_{re}$ and $\omega^{-1/2}$ in the low-frequency region, where $\omega$ is the angular frequency ($\omega = 2\pi f$). The less steep slope at the low-frequency region indicated higher $Na^+$ ion diffusivity in the $WSe_2$-rGO composite

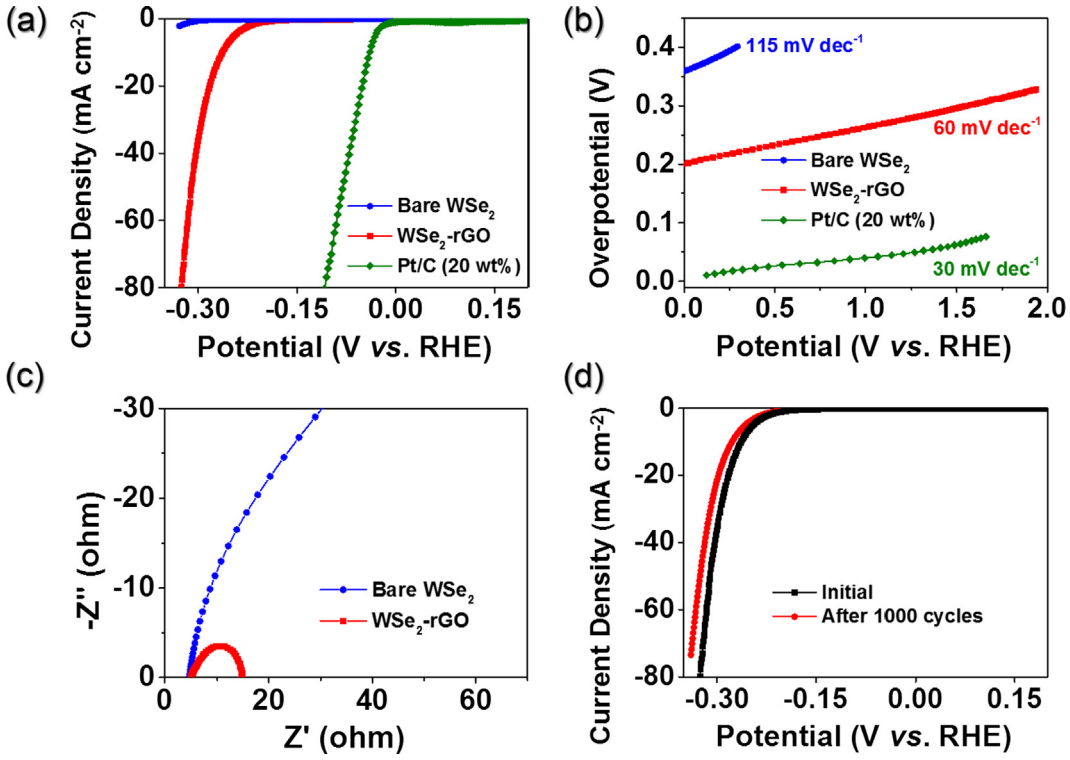


**Fig. 8.** Electrocatalytic performances of the $WSe_2$-rGO hybrid, bare $WSe_2$ and Pt/C composite particles: (a) polarization curves, (b) Tafel plots, (c) Nyquist plots, and (d) stability of the $WSe_2$-rGO hybrid.

particles [44]. The $WSe_2$-rGO composite particles had a faster $Na^+$ ion diffusion rate than the bare $WSe_2$ particles before cycling. The $R_{ct}$ values of the two samples decreased abruptly after the first cycle because of the formation of ultrafine nanocrystals during the first cycle, which was also observed in the previous reports [27,32]. The $R_{ct}$ values of the bare $WSe_2$ particles increased with increasing number of cycles, in which the $R_{ct}$ values at 1, 50, and 100 cycles were 108, 58, and 188 Ω, respectively (Fig. 7c). However, the $R_{ct}$ values of the $WSe_2$-rGO composite particles did not increase during the 100 cycles, in which the $R_{ct}$ values were 138, 84, and 85 Ω at 1, 50, and 100 cycles, respectively, as shown in Fig. 7d. The EIS results revealed the structural stability of the $WSe_2$-rGO composite particles during the repeated $Na^+$ ion insertion and extraction processes. In contrast, the structural destruction after 50 cycles increased the $R_{ct}$ values of the bare $WSe_2$ particles. Therefore, the fast $Na^+$ ion insertion and de-insertion and structural stability of the $WSe_2$-rGO composite improved the $Na^+$ ion storage properties.

We further investigated the electrocatalytic activity of the $WSe_2$-rGO composite particles by comparing them to that of the bare particles for the HER. Electrochemical measurements of the $WSe_2$–rGO composite, bare $WSe_2$, and Pt/C materials were carried out in 0.5 M $H_2SO_4$ using a three-electrode cell to study their HER activities (Fig. 8). In Fig. 8a, the Pt/C catalyst showed significantly high HER activity with a low onset potential (near zero), which is in good agreement with those of previous reports [45,46]. In contrast, the bare $WSe_2$ exhibited poor HER activity with a high negative onset potential, as well as low current density (0.61 mA $cm^{-2}$ at overpotential (η) = 300 mV), which can be attributed to the deficient number of active sites in $WSe_2$ because of its low surface area and low electrical conductivity [47,48]. Notably, the $WSe_2$-rGO composite particles showed much lower onset potential and larger current density (36.5 mA $cm^{-2}$ at η = 300 mV) than those of the bare $WSe_2$ particles, meaning that the composite particles showed prominent hydrogen evolution behavior with a large quantity of hydrogen evolution as well as low energy consumption. The results provide clear evidence that the addition of rGO is important for improving the electrocatalytic activity of $WSe_2$ catalysts.

To further investigate the HER activity of the $WSe_2$–rGO composite particles, the Tafel slope, which is concerned with the HER's rate-limiting step, was calculated by fitting the linear portions of Tafel plots with the Tafel equation (η = b log$j$ + a, where $j$ is the current density and b is the Tafel slope, Fig. 8b) [49–51]. The Tafel slopes for the Pt/C, bare $WSe_2$, and $WSe_2$–rGO composite were approximately 30, 115, and 60 mV $dec^{-1}$, respectively. The small Tafel slope value of the $WSe_2$–rGO composite particles suggested that the HER rate would rapidly increase as the overpotential increased, which is favorable for practical applications and is also superior or comparable to those reported for previous $WSe_2$-based composites (Table S2). According to one reported theory, with its Tafel slope of 60 mV $dec^{-1}$, the $WSe_2$–rGO composite particles catalyzed HER by the Volmer-Heyrovsky mechanism [52,53].

The bare $WSe_2$ and $WSe_2$–rGO composite particles were subjected to EIS to investigate the interface reactions and electrode kinetics during the HER (Fig. 8c). The small series resistances ($R_s$) were confirmed for all materials (~6 Ω), which may be the result of the electrolyte and wiring. The $R_{ct}$ arising from the electrode/electrolyte interface is related to the kinetic reaction rate [54,55]. Thus, compared with that of $WSe_2$, the higher $R_{ct}$ value of $WSe_2$-RGO hybrid implies that the RGO accelerates charge-transfer process for HER owing to its high conductivity.

The cycle durability of the HER catalysts is an important performance parameter for practical applications. Hence, the stability of the $WSe_2$–rGO composite particles was studied over 1000 cycles from 0.2 to −0.3 V (*vs.* RHE) with a scan rate of 0.1 V $s^{-1}$ (Fig. 8d). Despite a slight decrease in the current density (from 36.5 to 22.4 mA $cm^{-2}$ at η = 300 mV), the $WSe_2$–rGO composite particles nearly maintained the similar low onset potential, suggesting that these catalysts have a reasonable durability during long-term cycling.

To evaluate effective active sites for samples, electrochemical double-layer capacitance (EDLC, $C_{dl}$) were measured via CV method (Fig. 9). The CV shape of $WSe_2$-rGO composite is nearly rectangular compared to bare $WSe_2$, implying a fast electron and ion transport

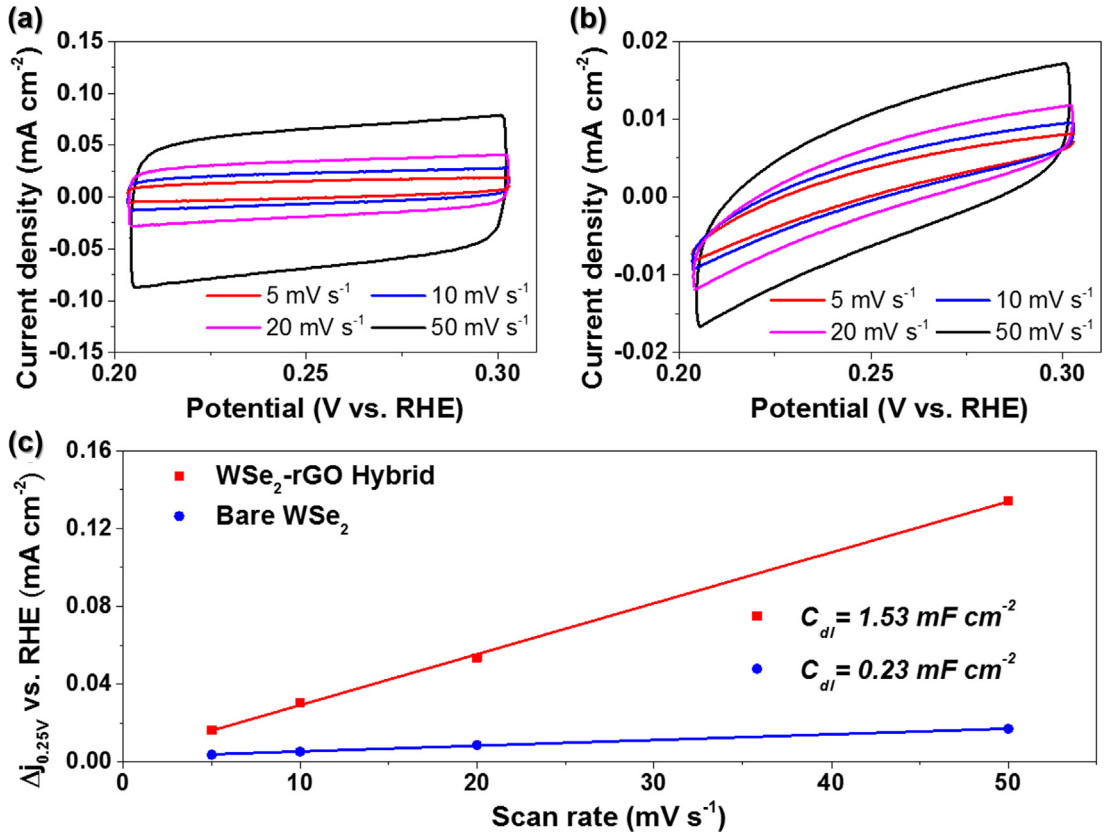


**Fig. 9.** Electrochemical double-layer capacitance results of (a) $WSe_2$-rGO composite, bare $WSe_2$ and (c) summary.

during potential sweep [55]. As shown in Fig. 9c, a linear trend was obtained by plotting the difference in current density at 0.25 V *vs.* RHE against scan rate. The $WSe_2$-rGO particles have larger EDLC value (1.53 mF $cm^{-2}$) compared with that of $WSe_2$ (0.23 mF $cm^{-2}$), indicating that the rGO is a critical factor determining the effective surface area in composites. In other words, the rGO in $WSe_2$-rGO composite could physically block the restacking of $WSe_2$ sheets, which results in improved electrochemical surface area. The large EDLC value suggests high exposure of electrochemical active sites, which is responsible for the great HER activity.

All of the performance results discussed above proved that $WSe_2$-rGO composite particles exhibit excellent catalytic activity with small overpotential [36.5 mA $cm^{-2}$ at $\eta = 300$ mV and Tafel slope (60 mV $dec^{-1}$)] as well as prominent durability. The improved electrochemical properties of $WSe_2$-rGO sample prove the synergistic effects between rGO and $WSe_2$. Based on the above results, there could be several plausible reasons to explain the improved electrochemical properties. First, fine $WSe_2$ nanocrystals, which were several nanometers in size, were uniformly distributed throughout the rGO nanosheets, resulting in the aggregation of $WSe_2$ nanosheets, thus providing more electrochemically active sites [56,57]. Second, the crumpled shape of the $WSe_2$–rGO composite powder particles improved the available surface area, affording high accessibility for electrolyte ions. Finally, the intimate contact between $WSe_2$ nanocrystals and rGO nanosheets could improve the electrical conductivity and stability of the composite materials, providing electron-transport pathway and structural integrity

## 4. Conclusions

The characteristics of the nanostructured mesoporous $WSe_2$-rGO composite particles with spherical and fine sized particles were compared to those of the bare $WSe_2$ particles prepared by the same process. The $WSe_2$-rGO composite particles showed superior cycling performance as the anode material for sodium-ion batteries compared to that of the bare $WSe_2$ particles. In addition, the $WSe_2$-rGO composite particles showed excellent catalytic activity with small overpotential and Tafel slope as well as prominent durability for the HER. The synergetic effect of ultrafine $WSe_2$ nanocrystals and well-dispersed rGO nanosheets resulted in superior electrochemical properties of sodium-ion batteries and electrocatalytic efficiencies for the HER.

## References

[1] S.Z. Butler, S.M. Hollen, L.Y. Cao, Y. Cui, J.A. Gupta, H.R. Gutierrez, T.F. Heinz, S.S. Hong, J.X. Huang, A.F. Ismach, E. Johnston-Halperin, M. Kuno, V.V. Plashnitsa, R.D. Robinson, R.S. Ruoff, S. Salahuddin, J. Shan, L. Shi, M.G. Spencer, M. Terrones, W. Windl, J.E. Goldberger, Progress, challenges, and opportunities in two-dimensional materials beyond graphene, ACS Nano 7 (2013) 2898–2926.
[2] M. Chhowalla, H.S. Shin, G. Eda, L.J. Li, K.P. Loh, H. Zhang, The chemistry of two-dimensional layered transition metal dichalcogenide nanosheets, Nat. Chem. 5 (2013) 263–275.
[3] G. Fiori, F. Bonaccorso, G. Iannaccone, T. Palacios, D. Neumaier, A. Seabaugh, S.K. Banerjee, L. Colombo, Electronics based on two-dimensional materials, Nat. Nanotechnol. 9 (2014) 768–779.
[4] Q.H. Wang, K. Kalantar-Zadeh, A. Kis, J.N. Coleman, M.S. Strano, Electronics and optoelectronics of two-dimensional transition metal dichalcogenides, Nat. Nanotechnol. 7 (2012) 699–712.
[5] M.S. Xu, T. Liang, M.M. Shi, H.Z. Chen, Graphene-like two-dimensional materials, Chem. Rev. 113 (2013) 3766–3798.
[6] Z.Y. Wang, J.T. Li, X.C. Tian, X.P. Wang, Y. Yu, K.A. Owusu, L. He, L.Q. Mai, Porous nickel-iron selenide nanosheets as highly efficient electrocatalysts for oxygen evolution reaction, ACS Appl. Mater. Interfaces 8 (2016) 19386–19392.
[7] N. Mahmood, C.Z. Zhang, Y.L. Hou, Nickel sulfide/nitrogen-doped graphene composites: phase-controlled synthesis and high performance anode materials for lithium ion batteries, Small 9 (2013) 1321–1328.
[8] A. Castellanos-Gomez, M. Barkelid, A.M. Goossens, V.E. Calado, H.S.J. van der Zant, G.A. Steele, Laser-thinning of $MoS_2$: on demand generation of a single-layer semiconductor, Nano Lett. 12 (2012) 3187–3192.
[9] B.L. Li, J. Wang, H.L. Zou, S. Garaj, C.T. Lim, J. Xie, N.B. Li, D.T. Leong, Low-dimensional transition metal dichalcogenide nanostructures based sensors, Adv. Funct. Mater. 26 (2016) 7034–7056.
[10] H.Y. Park, S.R. Dugasani, D.H. Kang, J. Jeon, S.K. Jang, S. Lee, Y. Roh, S.H. Park,

J.H. Park, N- and p-Type doping phenomenon by artificial DNA and m-DNA on two-dimensional transition metal dichalcogenides, ACS Nano 8 (2014) 11603–11613.
[11] D. Sarkar, X.J. Xie, J.H. Kang, H.J. Zhang, W. Liu, J. Navarrete, M. Moskovits, K. Banerjee, Functionalization of transition metal dichalcogenides with metallic nanoparticles: implications for doping and gas-sensing, Nano Lett. 15 (2015) 2852–2862.
[12] R.J. Chen, T. Zhao, W.P. Wu, F. Wu, L. Li, J. Qian, R. Xu, H.M. Wu, H.M. Albishri, A.S. Al-Bogami, D. Abd El-Hady, J. Lu, K. Amine, Free-standing hierarchically sandwich-type tungsten disulfide nanotubes/graphene anode for lithium-ion batteries, Nano Lett. 14 (2014) 5899–5904.
[13] Z. Gholamvand, D. McAteer, C. Backes, N. McEvoy, A. Harvey, N.C. Berner, D. Hanlon, C. Bradley, I. Godwin, A. Rovetta, M.E.G. Lyons, G.S. Duesberg, J.N. Coleman, Comparison of liquid exfoliated transition metal dichalcogenides reveals $MoSe_2$ to be the most effective hydrogen evolution catalyst, Nanoscale 8 (2016) 5737–5749.
[14] S. Mao, Z.H. Wen, S.Q. Ci, X.R. Guo, K. Ostrikov, J.H. Chen, Perpendicularly oriented $MoSe_2$/graphene nanosheets as advanced electrocatalysts for hydrogen evolution, Small 11 (2015) 414–419.
[15] Y.F. Shi, C.X. Hua, B. Li, X.P. Fang, C.H. Yao, Y.C. Zhang, Y.S. Hu, Z.X. Wang, L.Q. Chen, D.Y. Zhao, G.D. Stucky, Highly ordered mesoporous crystalline $MoSe_2$ material with efficient visible-light-driven photocatalytic activity and enhanced lithium storage performance, Adv. Funct. Mater. 23 (2013) 1832–1838.
[16] D. Voiry, H. Yamaguchi, J.W. Li, R. Silva, D.C.B. Alves, T. Fujita, M.W. Chen, T. Asefa, V.B. Shenoy, G. Eda, M. Chhowalla, Enhanced catalytic activity in strained chemically exfoliated $WS_2$ nanosheets for hydrogen evolution, Nat. Mater. 12 (2013) 850–855.
[17] H. Wang, X.Y. Wang, L. Wang, J. Wang, D.L. Jiang, G.P. Li, Y. Zhang, H.H. Zhong, Y. Jiang, Phase transition mechanism and electrochemical properties of nanocrystalline $MoSe_2$ as anode materials for the high performance lithium-ion Battery, J. Phys. Chem. C 119 (2015) 10197–10205.
[18] Y. Wang, D. Kong, W. Shi, B. Liu, G.J. Sim, Q. Ge, H.Y. Yang, Ice Templated free-standing hierarchically $WS_2$/CNT-rGO aerogel for high-performance rechargeable lithium and sodium ion batteries, Adv. Energy Mater. (2016) 1601057.
[19] Z. Hu, L.X. Wang, K. Zhang, J.B. Wang, F.Y. Cheng, Z.L. Tao, J. Chen, $MoS_2$ nanoflowers with expanded interlayers as high-performance anodes for sodium-ion batteries, Angew. Chem. Int. Ed. 53 (2014) 12794–12798.
[20] M. Traving, M. Boehme, L. Kipp, M. Skibowski, F. Starrost, E.E. Krasovskii, A. Perlov, W. Schattke, Electronic structure of $WSe_2$: a combined photoemission and inverse photoemission study, Phys. Rev. B 55 (1997) 10392–10399.
[21] W.J. Zhao, Z. Ghorannevis, L.Q. Chu, M.L. Toh, C. Kloc, P.H. Tan, G. Eda, Evolution of electronic structure in atomically thin sheets of $WS_2$ and $WSe_2$, ACS Nano 7 (2013) 791–797.
[22] K. Share, J. Lewis, L. Oakes, R.E. Carter, A.P. Cohn, C.L. Pint, Tungsten diselenide ($WSe_2$) as a high capacity, low overpotential conversion electrode for sodium ion batteries, RSC Adv. 5 (2015) 101262–101267.
[23] Z.A. Zhang, X. Yang, Y. Fu, Nanostructured $WSe_2$/C composites as anode materials for sodium-ion batteries, RSC Adv. 6 (2016) 12726–12729.
[24] H.T. Wang, D.S. Kong, P. Johanes, J.J. Cha, G.Y. Zheng, K. Yan, N.A. Liu, Y. Cui, $MoSe_2$ and $WSe_2$ nanofilms with vertically aligned molecular layers on curved and rough surfaces, Nano Lett. 13 (2013) 3426–3433.
[25] Z.Q. Liu, H.Y. Zhao, N. Li, Y. Zhang, X.Y. Zhang, Y.P. Du, Assembled 3D electrocatalysts for efficient hydrogen evolution: $WSe_2$ layers anchored on graphene sheets, Inorg. Chem. Front. 3 (2016) 313–319.
[26] J.S. Cho, S.Y. Lee, Y.C. Kang, First introduction of $NiSe_2$ to anode material for sodium-ion batteries: a hybrid of graphene-wrapped $NiSe_2$/C porous nanofiber, Sci. Rep. 6 (2016) 23338.
[27] G.D. Park, J.S. Cho, Y.C. Kang, Sodium-ion storage properties of nickel sulfide hollow nanospheres/reduced graphene oxide composite particles prepared by a spray drying process and the nanoscale Kirkendall effect, Nanoscale 7 (2015) 16781–16788.
[28] A. Ambrosi, Z. Sofer, M. Pumera, 2H - > 1T phase transition and hydrogen evolution activity of $MoS_2$, $MoSe_2$, $WS_2$ and $WSe_2$ strongly depends on the $MX_2$ composition, Chem. Commun. 51 (2015) 8450–8453.
[29] J.K. Huang, J. Pu, C.L. Hsu, M.H. Chiu, Z.Y. Juang, Y.H. Chang, W.H. Chang, Y. Iwasa, T. Takenobu, L.J. Li, Large-area synthesis of highly crystalline $WSe_2$ mono layers and device applications, ACS Nano 8 (2014) 923–930.
[30] T.H. Fleisch, G.J. Mains, An XPS Study of the UV Reduction and Photochromism of $MoO_3$ and $WO_3$, J. Chem. Phys. 76 (1982) 780–786.
[31] X.F. Chen, Y. Huang, K.C. Zhang, X.S. Feng, M.Y. Wang, Synthesis and high-performance of carbonaceous polypyrrole nanotubes coated with $SnS_2$ nanosheets anode materials for lithium ion batteries, Chem. Eng. J. 330 (2017) 470–479.
[32] G.D. Park, J.S. Cho, Y.C. Kang, Novel cobalt oxide-nanobubble-decorated reduced graphene oxide sphere with superior electrochemical properties prepared by nanoscale Kirkendall diffusion process, Nano Energy 17 (2015) 17–26.
[33] A.C. Ferrari, J.C. Meyer, V. Scardaci, C. Casiraghi, M. Lazzeri, F. Mauri, S. Piscanec, D. Jiang, K.S. Novoselov, S. Roth, A.K. Geim, Raman spectrum of graphene and graphene layers, Phys. Rev. Lett. 97 (2006) 187401.
[34] Y.A. Xu, Q.L. Wei, C. Xu, Q.D. Li, Q.Y. An, P.F. Zhang, J.Z. Sheng, L. Zhou, L.Q. Mai, Layer-by-Layer $Na_3V_2(PO_4)_3$ Embedded in reduced graphene oxide as superior rate and ultralong-life sodium-ion battery cathode, Adv. Energy Mater. 6 (14) (2016) 1600389.
[35] X.F. Chen, Y. Huang, K.C. Zhang, X.S. Feng, M.Y. Wang, Porous $TiO_2$ nanobelts coated with mixed transition-metal oxides $Sn_3O_4$ nanosheets core-shell composites as high-performance anode materials of lithium ion batteries, Electrochim. Acta 259 (2018) 131–142.
[36] P.A. Monson, Understanding adsorption/desorption hysteresis for fluids in mesoporous materials using simple molecular models and classical density functional theory, Micropor. Mesopor. Mat. 160 (2012) 47–66.
[37] J.S. Cho, J.M. Won, J.H. Lee, Y.C. Kang, Synthesis and electrochemical properties of spherical and hollow-structured NiO aggregates created by combining the Kirkendall effect and Ostwald ripening, Nanoscale 7 (2015) 19620–19626.
[38] Y.M. Sun, X.L. Hu, W. Luo, F.F. Xia, Y.H. Huang, Reconstruction of conformal nanoscale MnO on graphene as a high-capacity and long-life anode material for lithium ion batteries, Adv. Funct. Mater. 23 (2013) 2436–2444.
[39] H. Wu, M. Xu, Y.C. Wang, G.F. Zheng, Branched $Co_3O_4$/$Fe_2O_3$ nanowires as high capacity lithium-ion battery anodes, Nano Res. 6 (2013) 167–173.
[40] H. Wu, M. Xu, H.Y. Wu, J.J. Xu, Y.L. Wang, Z. Peng, G.F. Zheng, Aligned NiO nanoflake arrays grown on copper as high capacity lithium-ion battery anodes, J. Mater. Chem. 22 (2012) 19821–19825.
[41] J.S. Cho, Y.J. Hong, Y.C. Kang, Design and synthesis of bubble-nanorod-structured $Fe_2O_3$-carbon nanofibers as advanced anode material for Li-ion batteries, ACS Nano 9 (2015) 4026–4035.
[42] X.F. Chen, Y. Huang, K.C. Zhang, W.C. Zhang, Cobalt fibers anchored with tin disulfide nanosheets as high-performance anode materials for lithium ion batteries, J. Colloid Interface Sci. 506 (2017) 291–299.
[43] X.F. Chen, Y. Huang, K.C. Zhang, Cobalt nanofibers coated with layered nickel silicate coaxial core-shell composites as excellent anode materials for lithium ion batteries, J. Colloid Interface Sci. 513 (2018) 788–796.
[44] G.Q. Liu, H.T. Kuo, R.S. Liu, C.H. Shen, D.S. Shy, X.K. Xing, J.M. Chen, Study of electrochemical properties of coating $ZrO_2$ on $LiCoO_2$, J. Alloy Compd. 496 (2010) 512–516.
[45] Y. Yin, J.C. Han, Y.M. Zhang, X.H. Zhang, P. Xu, Q. Yuan, L. Samad, X.J. Wang, Y. Wang, Z.H. Zhang, P. Zhang, X.Z. Cao, B. Song, S. Jin, Contributions of phase, sulfur vacancies, and edges to the hydrogen evolution reaction catalytic activity of porous molybdenum disulfide nanosheets, J. Am. Chem. Soc. 138 (2016) 7965–7972.
[46] S. Reddy, R. Du, L.X. Kang, N.N. Mao, J. Zhang, Three dimensional CNTs aerogel/MoSx as an electrocatalyst for hydrogen evolution reaction, Appl. Catal. B-Environ. 194 (2016) 16–21.
[47] M.L. Zou, J.F. Zhang, H. Zhu, M.L. Du, Q.F. Wang, M. Zhang, X.W. Zhang, A 3D dendritic $WSe_2$ catalyst grown on carbon nanofiber mats for efficient hydrogen evolution, J. Mater. Chem. A 3 (2015) 12149–12153.
[48] C. Tsai, K.R. Chan, F. Abild-Pedersen, J.K. Norskov, Active edge sites in $MoSe_2$ and $WSe_2$ catalysts for the hydrogen evolution reaction: a density functional study, Phys. Chem. Chem. Phys. 16 (2014) 13156–13164.
[49] F.X. Ma, H.B. Wu, B.Y. Xia, C.Y. Xu, X.W. Lou, Hierarchical beta-$Mo_2C$ nanotubes organized by ultrathin nanosheets as a highly efficient electrocatalyst for hydrogen production, Angew. Chem. Int. Ed. 54 (2015) 15395–15399.
[50] L.B. Ma, Y. Hu, G.Y. Zhu, R.P. Chen, T. Chen, H.L. Lu, Y.R. Wang, J. Liang, H.X. Liu, C.Z. Yan, Z.X. Tie, Z. Jin, J. Liu, In situ thermal synthesis of inlaid ultrathin $MoS_2$/graphene nanosheets as electrocatalysts for the hydrogen evolution reaction, Chem. Mater. 28 (2016) 5733–5742.
[51] A.L. Lu, Y.Z. Chen, H.Y. Li, A. Dowd, M.B. Cortie, Q.S. Xie, H.Z. Guo, Q.Q. Qi, D.L. Peng, Magnetic metal phosphide nanorods as effective hydrogen-evolution electrocatalysts, Int. J. Hydrogen Energy 39 (2014) 18919–18928.
[52] D.Y. Chung, S.K. Park, Y.H. Chung, S.H. Yu, D.H. Lim, N. Jung, H.C. Ham, H.Y. Park, Y. Piao, S.J. Yoo, Y.E. Sung, Edge-exposed $MoS_2$ nano-assembled structures as efficient electrocatalysts for hydrogen evolution reaction, Nanoscale 6 (2014) 2131–2136.
[53] Y.P. Huang, Y.E. Miao, L.S. Zhang, W.W. Tjiu, J.S. Pan, T.X. Liu, Synthesis of few-layered $MoS_2$ nanosheet-coated electrospun $SnO_2$ nanotube heterostructures for enhanced hydrogen evolution reaction, Nanoscale 6 (2014) 10673–10679.
[54] J.F. Xie, J.J. Zhang, S. Li, F. Grote, X.D. Zhang, H. Zhang, R.X. Wang, Y. Lei, B.C. Pan, Y. Xie, Controllable disorder engineering in oxygen-incorporated $MoS_2$ ultrathin nanosheets for efficient hydrogen evolution, J. Am. Chem. Soc. 135 (2013) 17881–17888.
[55] S.K. Park, D.Y. Chung, D. Ko, Y.E. Sung, Y. Piao, Three-dimensional carbon foam/N-doped graphene@$MoS_2$ hybrid nanostructures as effective electrocatalysts for the hydrogen evolution reaction, J. Mater. Chem. A 4 (2016) 12720–12725.
[56] J.F. Xie, H. Zhang, S. Li, R.X. Wang, X. Sun, M. Zhou, J.F. Zhou, X.W. Lou, Y. Xie, Defect-rich $MoS_2$ Ultrathin nanosheets with additional active edge sites for enhanced electrocatalytic hydrogen evolution, Adv. Mater. 25 (2013) 5807–5813.
[57] Y.G. Li, H.L. Wang, L.M. Xie, Y.Y. Liang, G.S. Hong, H.J. Dai, $MoS_2$ nanoparticles grown on graphene: an advanced catalyst for the hydrogen evolution reaction, J. Am. Chem. Soc. 133 (2011) 7296–7299.